ChemPubSoc Europe

DOI: 10.1002/cphc.201300842

# Spectroscopic Properties and Upconversion Studies in $Ho^{3+}/Yb^{3+}$ Co-doped Calcium Scandate with Spectrally Pure Green emission

Jing Li,[a, c] Jiahua Zhang,*[a] Zhendong Hao,[a] Xia Zhang,[a] Jihong Zhao,[b] and Yongshi Luo[a]

The optical properties of a $Ho^{3+}/Yb^{3+}$ co-doped $CaSc_2O_4$ oxide material are investigated in detail. The spectral properties are described as a function of doping concentrations. The efficient $Yb^{3+}\rightarrow Ho^{3+}$ energy transfer is observed. The transfer efficiency approaches 50% before concentration quenching. The concentration-optimized sample exhibits a strong green emission accompanied with a weak red emission, showing perfect green monochromaticity. The results of the spectral distribution, power dependence, and lifetime measurements are presented. The green, red, and near-infrared (NIR) emissions around 545, 660, and 759 nm are assigned to the $^5F_4+{}^5S_2\rightarrow{}^5I_8$, $^5F_5\rightarrow{}^5I_8$, and $^5F_4+{}^5S_2\rightarrow{}^5I_7$ transitions of $Ho^{3+}$, respectively. The detailed study reveals the upconversion luminescence mechanism involved in a novel $Ho^{3+}/Yb^{3+}$ co-doped $CaSc_2O_4$ oxide material.

## 1. Introduction

The infrared-to-visible upconversion luminescence (UCL) of crystals doped with rare earth (RE) ions has attracted much attention during the past two decades, owing to its potential applications in display technologies, biological imaging, and sensitive biological fluorescent labeling, and so forth.[1–3] In particular, imaging science and technology has actively used RE-metal-doped crystals as imaging probes because of their weak autofluorescence, deep penetration of noninvasive near-infrared (NIR) excitation, and low radiation damage.[3–5] However, the overlapping emission bands of RE ions hinder the simultaneous tracking of multiple fluorescent probes, which requires UCL to have a spectrally pure emission.[3,4,6] Among RE ions, $Ho^{3+}$ is one of the most important active ions, owing to its excellent green and red UCL.[7,8] Combination of $Ho^{3+}$ with $Yb^{3+}$ can further enhance the emission efficiency.[8] $Ho^{3+}/Yb^{3+}$ combinations are recognized as excellent green UCL emitters under the NIR beam issued from a 980 nm laser diode (LD) excitation. The predominant green UCL of $Ho^{3+}$ is usually obtained in low phonon energy hosts, that is, fluorides.[9–12] It is also strongly expected in oxide materials because of their stable chemical and thermal properties.[13,14] $CaSc_2O_4$ is a new and promising oxide host, which exhibits an orthorhombic $CaFe_2O_4$ structure that was firstly reported by Carter and Feigelson in 1964.[15] It has the low phonon frequency of 540 $cm^{-1}$. Our group have reported the intense UCL in $CaSc_2O_4$:$Tm^{3+}/Yb^{3+}$ samples, implying $CaSc_2O_4$ is an excellent host material for highly efficient UCL.[16,17] However, a detailed study regarding the UCL properties of $Ho^{3+}/Yb^{3+}$co-doped $CaSc_2O_4$ has not been provided yet.

In this work, the characterization of the structural and UCL properties of $CaSc_2O_4$:$Ho^{3+}/Yb^{3+}$ is detailed. The concentration dependence of the spectral distribution from 450 to 1300 nm is researched in detail. Concentration-optimized $CaSc_2O_4$:$Ho^{3+}/Yb^{3+}$ phosphor presents efficient $Yb^{3+}\rightarrow Ho^{3+}$ energy transfer and perfect green monochromaticity. The UCL mechanism is analyzed through spectral distributions, power dependences, and lifetime measurements. The experimental results are in good agreement with theoretical analyses. Discussions on the optical properties of $CaSc_2O_4$:$Ho^{3+}/Yb^{3+}$ are conducive to broaden the understanding of this novel material as a promising oxide host for simultaneous tracking of multiple upconverting probes.

## 2. Results and Discussion

### 2.1 Structure and Luminescence Spectroscopy of the $CaSc_2O_4$:$Ho^{3+}/Yb^{3+}$ Phosphor

Figure 1 shows the results of Rietveld refinement for $CaSc_2O_4$:0.2%$Ho^{3+}$,10%$Yb^{3+}$ sample. The initial structural model was constructed with crystallographic data for $CaSc_2O_4$ (JCPDS 20-0234).[15] All observed X-ray diffraction (XRD) peaks are obtained with the fit parameters of the profile *R*-factor ($R_p=2.65\%$) and the weighted profile *R*-factor ($R_{wp}=4.35\%$), indicating that a relatively pure phase was obtained. The inset of Figure 1 shows the schematic crystal structure of $CaSc_2O_4$. The coordination numbers for $Ca^{2+}$ and $Sc^{3+}$ are eight and six, respectively. For $Sc^{3+}$, there are two coordinated sites in $CaSc_2O_4$. The host lattice exhibits the space group *Pnam* (62),

[a] Dr. J. Li, Prof. J. Zhang, Dr. Z. Hao, X. Zhang, Dr. Y. Luo
State Key Laboratory of Luminescence and Applications
Changchun Institute of Optics, Fine Mechanics and Physics
Chinese Academy of Sciences, 3888 Eastern South Lake Road
Changchun 130033 (PR China)
Fax: (+86) 431-8617-6317
E-mail: zhangjh@ciomp.ac.cn

[b] Dr. J. Zhao
Jilin Cancer Hospital, 1018 Huguang Road, Changchun 130012 (PR China)

[c] Dr. J. Li
University of Chinese Academy of Sciences, Beijing, 100039 (PR China)

 © 2013 Wiley-VCH Verlag GmbH & Co. KGaA, Weinheim 

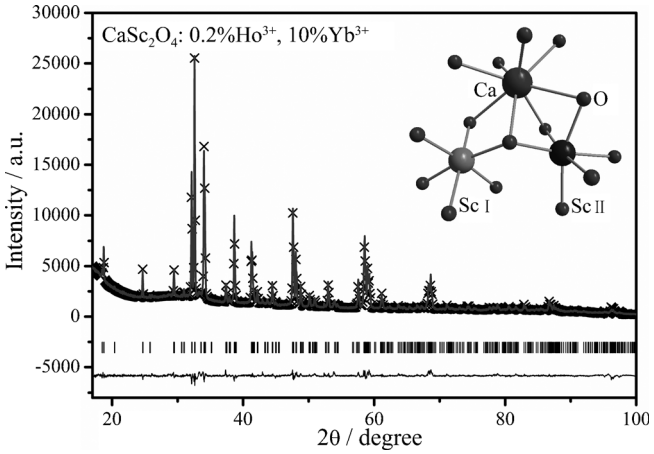


**Figure 1.** Experimental, calculated, and difference results of the XRD refinement for $CaSc_2O_4$:$Ho^{3+}$/$Yb^{3+}$.

with cell parameters: $a = 9.4693(7)$ Å, $b = 11.1336(8)$ Å, and $c = 3.1500(8)$ Å. The lattice parameters obtained in the doped sample are slightly larger than those in the pure phase, indicating that the $Yb^{3+}$ ions with a larger ionic radius (0.868 Å) occupy the $Sc^{3+}$ (0.745 Å) sites.[20]

The room-temperature visible luminescence spectra of $CaSc_2O_4$:0.2%$Ho^{3+}$, 10%$Yb^{3+}$ excited at 454 and 980 nm are shown in Figure 2. Following 980 nm excitation (bottom), the

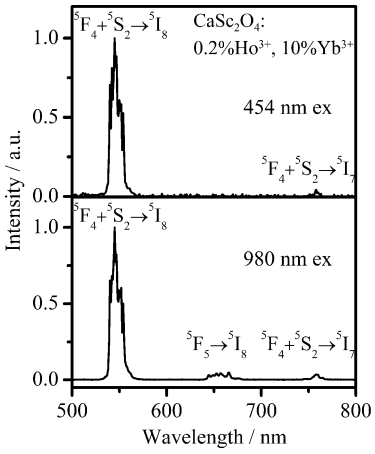


**Figure 2.** Room-temperature emission spectra of $CaSc_2O_4$:$Ho^{3+}$/$Yb^{3+}$, excited at 454 nm (top) and 980 nm (bottom).

spectrum exhibits three UCL emissions, peaked around 545, 660, and 759 nm, which are assigned to the $^5F_4 + {}^5S_2 \rightarrow {}^5I_8$, $^5F_5 \rightarrow {}^5I_8$, and $^5F_4 + {}^5S_2 \rightarrow {}^5I_7$ transitions of $Ho^{3+}$, respectively. Under 454 nm excitation (top), the red (660 nm) emission, corresponding to the direct excitation of $Ho^{3+}$:$^3K_8$, disappears and only the green (545 nm) and NIR (759 nm) emissions are observed. The intensity ratio of green-to-NIR emission does not vary with the excitation wavelength.

### 2.2 Concentration Dependence of the Emission Spectra

The UCL spectra of $CaSc_2O_4$:x$Ho^{3+}$,10%$Yb^{3+}$ ($x = 0.05$, 0.1, 0.2, 0.4, 0.8, 1.2, and 1.6%) under 980 nm excitation are presented in Figure 3a. For a fixed $Yb^{3+}$ concentration at 10%, the strongest green UCL is observed for a $Ho^{3+}$ concentration around 0.2%. For $Ho^{3+}$ concentrations over 0.2%, the intensity begins to diminish because of the cross-relaxation processes of $Ho^{3+}$.[14,21] Figure 3b shows the relative intensity of the red emissions, which have a slight enhancement as the $Ho^{3+}$ concentration is increasing. The intensity ratio of green-to-NIR

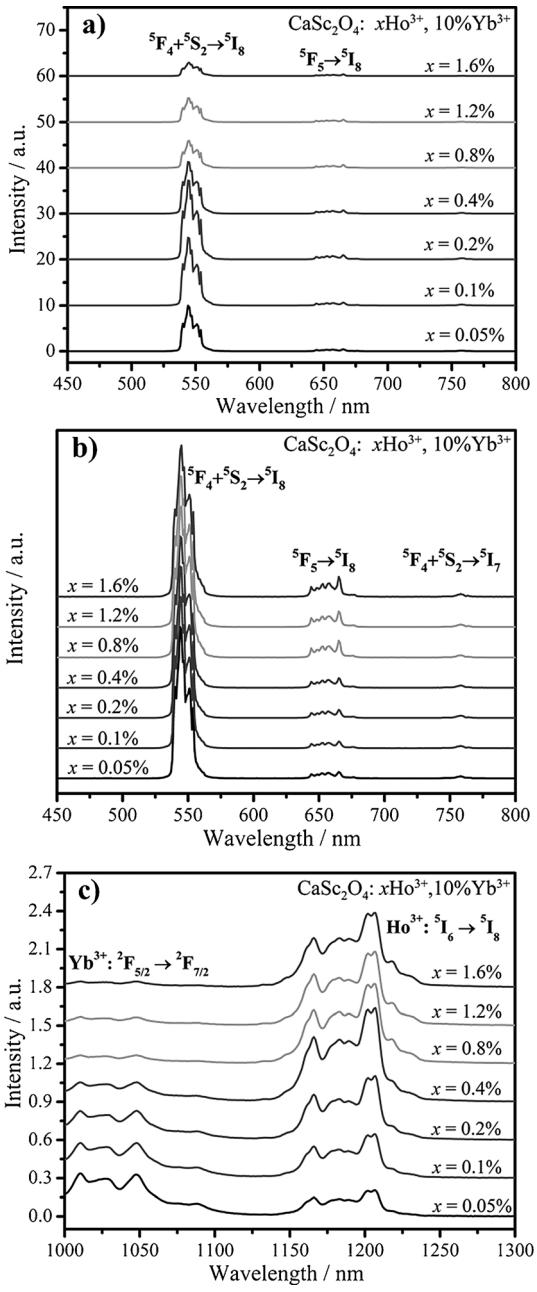


**Figure 3.** a) UCL spectra, b) UCL spectra normalized to the green emission, and c) UCL spectra normalized to the infrared emission for $CaSc_2O_4$: x$Ho^{3+}$,10%$Yb^{3+}$ ($x = 0.05$, 0.1, 0.2, 0.4, 0., 1.2, and 1.6%) under 980 nm excitation.

© 2013 Wiley-VCH Verlag GmbH & Co. KGaA, Weinheim

emissions does not vary with $Ho^{3+}$ concentration. Figure 3c shows the infrared emission spectra from 1000 to 1300 nm of the same samples. The spectra show typical $Yb^{3+}$:$^2F_{5/2}\rightarrow{}^2F_{7/2}$ emissions around 1050 nm and $Ho^{3+}$:$^5I_6\rightarrow{}^5I_8$ emissions around 1200 nm. As the $Ho^{3+}$ concentration is increasing, the $Yb^{3+}$ emission at 1050 nm exhibits a monotonic decline. It is considered an indication of efficient $Yb^{3+}\rightarrow Ho^{3+}$ energy transfer. The $Ho^{3+}$ emission at 1200 nm reaches a maximum when $x=0.4\%$. For higher $Ho^{3+}$ concentrations, the intensity declines as a result of the self-absorption of $Ho^{3+}$.[22]

The UCL (450–800 nm) and infrared (1000–1300 nm) emission spectra of $CaSc_2O_4$:0.2%$Ho^{3+}$,y$Yb^{3+}$ ($y=1$, 2, 6, 10, 14, 18, 22, and 26%) are presented in Figure 4. For the optimal $Ho^{3+}$

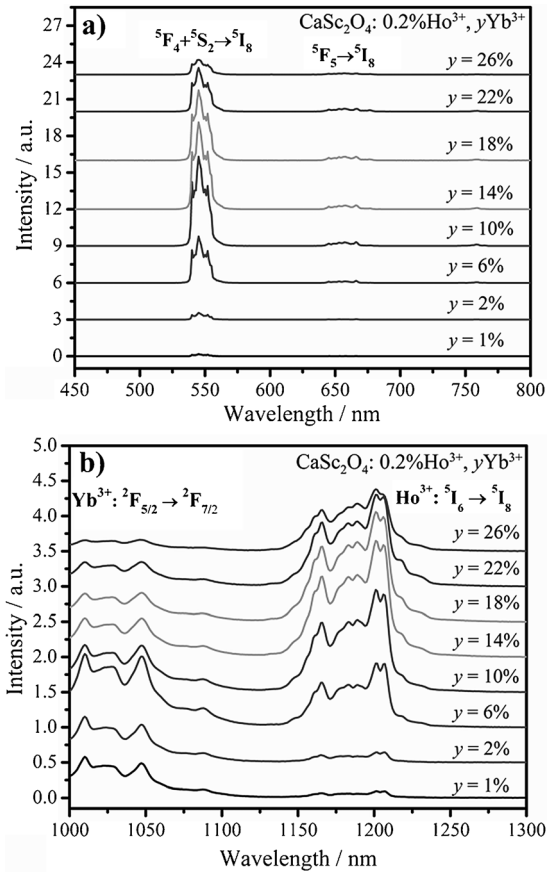


**Figure 4.** a) UCL spectra and b) infrared emission spectra of $CaSc_2O_4$: 0.2%$Ho^{3+}$,y$Yb^{3+}$ ($y=1$, 2, 6, 10, 14, 18, 22, 26%) under 980 nm excitation.

concentration of 0.2%, the green emission exhibits the strongest luminescence when the $Yb^{3+}$ concentration is 10%. In the infrared region, the $Ho^{3+}$ emission at 1200 nm reaches a maximum when $y=14\%$. The optimal $Yb^{3+}$ concentration for green UCL (10%) is lower than that for the 1200 nm emission (14%) of $Ho^{3+}$, owing to $Ho^{3+}\rightarrow Yb^{3+}$ back-energy transfer process.[17,23,24]

### 2.3 Pump-Power Dependence of Emission Intensities

The 980 nm pump-power dependence of the $Yb^{3+}$:$^2F_{5/2}\rightarrow{}^2F_{7/2}$ (1050 nm), $Ho^{3+}$:$^5I_6\rightarrow{}^5I_8$ (1200 nm), $^5F_5\rightarrow{}^5I_8$ (660 nm), $^5F_4+{}^5S_2\rightarrow{}^5I_7$ (759 nm), and $^5F_4+{}^5S_2\rightarrow{}^5I_8$ (545 nm) emissions were measured and plotted in double logarithmic scales, as shown in Figure 5. The focus area of the pumping beam was

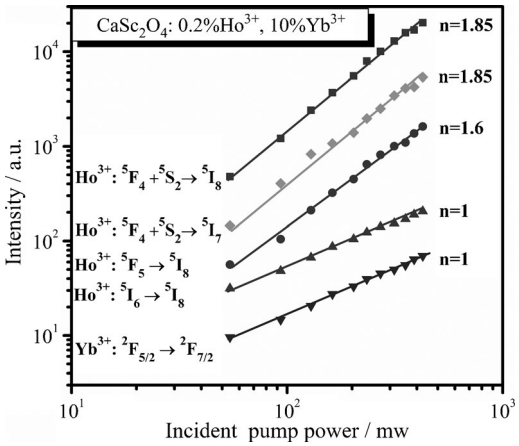


**Figure 5.** Pump-power dependence of emission intensities in $CaSc_2O_4$:$Ho^{3+}$/$Yb^{3+}$ under the 980 nm pump.

fixed at about 80 $mm^2$. The number of 980 nm photons required to absorb for emitting one given photon is denoted *n*. Due to the competition between linear decay and upconversion of the excited state, the experimental *n* value becomes smaller than the theoretical one.[25] The linear decay is dominant under low pump-power density, which is used in our experiment. The *n* value for the five emissions is 1, 1, 1.6, 1.85, and 1.85, which indicates the number (1, 1, 2, 2, 2, respectively) of pump steps that is required to populate the corresponding emitting level. The population saturation is not found for the $Ho^{3+}$:$^5I_6$ level. The same *n* value of both the 545 and 759 nm emissions reflects that they originate from the same excited state ($^5F_4+{}^5S_2$), which is confirmed in the spectrum distribution because the intensity ratio of the two emissions does not vary with the excitation wavelengths or the doped concentrations. The *n* value for the 660 nm red emission is smaller than that for 545 nm green emission. The $^5F_5$ level generating red emissions is predominately populated through other mechanisms, rather than nonradiation from the upper ($^5F_4+{}^5S_2$) states.

### 2.4 Lifetime Measurements

The time evolutions of the green (545 nm), red (660 nm), and NIR (759 nm) UCL emissions under pulsed 980 nm excitation in $CaSc_2O_4$:0.2%$Ho^{3+}$,10%$Yb^{3+}$ are presented in Figure 6. Each transient exhibits a typical rise and decay. This is a clear indication of the energy-transfer process. It is worth noting that the green and NIR emissions have a similar rise and decay process. The red emission has a slower rise and decay. The simplified model predicts that the time dependence of the UCL emission

© 2013 Wiley-VCH Verlag GmbH & Co. KGaA, Weinheim

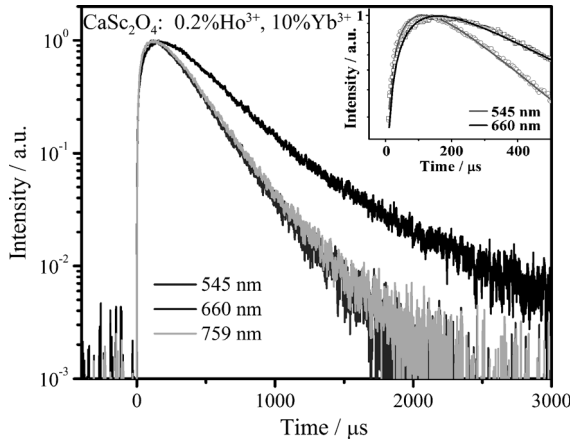


**Figure 6.** Time evolutions of the green (545 nm), red (660 nm), and NIR (759 nm) emissions under pulsed 980 nm excitation in $CaSc_2O_4$:$Ho^{3+}$/$Yb^{3+}$. Inset: an expansion of the green and red initial rise processes.

intensity, $I(t)$, can be proposed after a short pulse of excitation [Eq. (1)]:[26]

$$I(t) = A(e^{-t/\tau_d} - e^{-t/\tau_r}) \quad (1)$$

in which $A$ is an emission intensity factor and $\tau_r$ and $\tau_d$ represent the rise and decay times of the transient, respectively. The decay times for the green, red, and NIR emissions are calculated by integrating the area under the corresponding decay curves with the normalized initial intensity, reaching $\tau_d = 249$, 397, and 253 μs, respectively.

The best fit for the green and red emission achieve $\tau_r$ values of 61.5 and 77.3 μs, respectively, as shown in the inset of Figure 6. The short $\tau_r$ is decided by the self-decay of level. The long $\tau_d$ may depend mainly on the lifetimes of the $Yb^{3+}$:$^2F_{5/2}$ level and intermediate states of $Ho^{3+}$ in the $CaSc_2O_4$ host. The slower decay for red emission is due to its intermediate state ($^5I_7$), which is more stable than that of the green emission ($^5I_6$).

### 2.5 UCL Mechanism

By combining the spectrum distribution, slope $n$, and decay curves, the upconversion pathways in $CaSc_2O_4$:$Ho^{3+}$/$Yb^{3+}$ can be demonstrated schematically, as shown in Figure 7. Through two successive $Yb^{3+}$ to $Ho^{3+}$ energy-transfer steps, $Yb^{3+}$:$^2F_{5/2}$ + $Ho^{3+}$:$^5I_8$ → $Yb^{3+}$:$^2F_{7/2}$ + $Ho^{3+}$:$^5I_6$ and $Yb^{3+}$:$^2F_{5/2}$ + $Ho^{3+}$:$^5I_6$ → $Yb^{3+}$:$^2F_{7/2}$ + $Ho^{3+}$:($^5F_4$ + $^5S_2$), the ($^5F_4$ + $^5S_2$) levels are populated. The green and NIR emissions are found by $^5F_4 + {}^5S_2 \rightarrow {}^5I_8$ and $^5F_4 + {}^5S_2 \rightarrow {}^5I_7$, respectively. The red emission is from the $Ho^{3+}$:$^5F_5$ level. The $^5F_5$ state is populated through $^5I_6 \rightarrow {}^5I_7$ nonradiative relaxation and subsequent $Yb^{3+}$:$^2F_{5/2}$ + $Ho^{3+}$:$^5I_7$ → $Yb^{3+}$:$^2F_{7/2}$ + $Ho^{3+}$:$^5F_5$ energy transfer. The $^5I_7$ level has a long lifetime,[27] exhibiting remarkable saturation on its power dependence.[28] It is easy to reach saturation for the red emission, which shows a smaller $n$ value than the green emission.

According to upconversion pathways, the steady-state rate Equations are given by Equations (2)–(6):

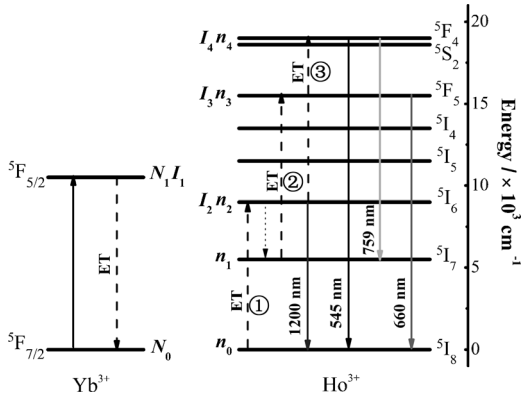


**Figure 7.** Energy-level diagrams and energy-transfer pathways in $CaSc_2O_4$:$Ho^{3+}$/$Yb^{3+}$.

$$\frac{dn_1}{dt} = W_n 21 n_2 + W_{41} n_4 - \frac{n_1}{\tau_1} - C_2 N_1 n_1, \quad (2)$$

$$\frac{dn_2}{dt} = C_1 N_1 n_0 - W_n 21 n_2 - \frac{n_2}{\tau_2} - C_3 N_1 n_2, \quad (3)$$

$$\frac{dn_3}{dt} = C_2 N_1 n_1 - \frac{n_3}{\tau_3}, \quad (4)$$

$$\frac{dn_4}{dt} = C_3 N_1 n_2 - \frac{n_4}{\tau_4}, \quad (5)$$

$$\frac{dN1}{dt} = \sigma I N_0 - C_1 N_1 n_0 - C_2 N_1 n_1 - C_3 N_1 n_2 - \frac{N_1}{\tau_{Yb}}. \quad (6)$$

in which $\sigma$ is the absorption cross section of the $Yb^{3+}$ ion, $I$ is the incident pumping power, $N_i$ is the population of $i_{th}$ level of $Yb^{3+}$, $n_i$ is the population of $i_{th}$ level of $Ho^{3+}$ involved in the upconversion process, $C_i$ represents the $Yb^{3+} \rightarrow Ho^{3+}$ energy-transfer coefficient for steps $i = 1$, 2, 3, $W_{ij}$ and $W_{nij}$ represent the radiative and nonradiative rate between $i$ and $j$ levels of the $Ho^{3+}$ ion, respectively, $\tau_i$ is the measured lifetime of the $i_{th}$ level of $Ho^{3+}$, and $\tau_{Yb}$ is that of the $Yb^{3+}$:$^2F_{5/2}$ level. For samples with a very low $Ho^{3+}$ concentration, the cross relaxation of Ho–Ho interaction is assumed to be negligible.[7] The excitations of $Ho^{3+}$ by energy transfer to higher levels are neglected due to the weak pump in our experiment. According to the faint emission of $^5F_4 + {}^5S_2 \rightarrow {}^5I_7$ shown in the UCL spectra, the $^5I_7$ population is mostly from the nonradiative transition of $^5I_6$. Considering the small branching ratio of the $Ho^{3+}$:$^5I_6 \rightarrow {}^5I_7$ transition[27] and the intense $^5I_6 \rightarrow {}^5I_8$ emission around 1200 nm in the infrared spectra, the $Ho^{3+}$:$^5I_6$ level is depopulated by $^5I_6 \rightarrow {}^5I_8$ radiative transition, rather than alternative $^5I_6 \rightarrow {}^5I_7$ nonradiation.

According to Equations (2) and (3), a general physical description of the intensity ratio ($I_2/I_1$) of the $Ho^{3+}$:$^5I_6$ to $Yb^{3+}$:$^2F_{5/2}$ emission can be derived by using Equation (7):

$$\frac{I_2}{I_1} = \frac{\gamma_2 n_2}{\gamma_1 N_1} = \frac{C_1 \gamma_2 n_0}{\gamma_1 \tau_2^{-1} + C_3 \gamma_1 N_1} \quad (7)$$

in which $I_i$ and $\gamma_i$ represent the emission intensity and radiative rate, respectively, for the $Yb^{3+}$:$^2F_{5/2}$, $Ho^{3+}$:$^5I_6$, $^5F_5$, and ($^5F_4 + {}^5S_2$)

© 2013 Wiley-VCH Verlag GmbH & Co. KGaA, Weinheim

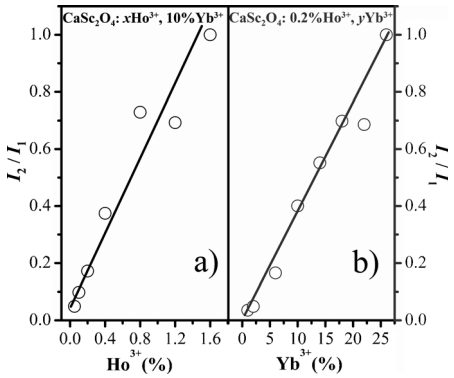


**Figure 8.** Evolution of intensity ratio $I_2/I_1$ as a function of a) $Ho^{3+}$ and b) $Yb^{3+}$ concentration.

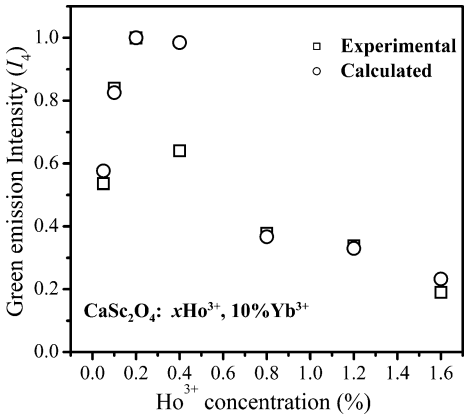


**Figure 9.** Calculated and experimental green emission intensities ($I_4$) at various $Ho^{3+}$ concentrations. The intensities are scaled to the maximum.

levels. The $\gamma_i$ values are constants. Figure 8a shows that the $I_2/I_1$ value exhibits a proportional relationship with the $Ho^{3+}$ concentration ($n_0$). The $\tau_2$ of $Ho^{3+}$:$^5I_6$ is almost fixed, owing to the faint nonradiation relaxation. It indicates that the energy-transfer coefficient $C_1$ is constant when the $Yb^{3+}$ concentration is fixed. The $I_2/I_1$ also exhibits linear dependence with the $Yb^{3+}$ concentration, as shown in Figure 8b. Because the $Ho^{3+}$ concentration is very low (0.2%), few excited $Yb^{3+}$ ions are within the critical transfer distance of $Ho^{3+}$. In such a situation, $Yb^{3+} \rightarrow Ho^{3+}$ energy transfer is the diffusion-limited relaxation process.[23,29] The nearest distance of Yb–Yb is only 3.19 Å in the $CaSc_2O_4$ sample.[16] As the $Yb^{3+}$ concentration increases, the energy migration among $Yb^{3+}$ ions gradually enhances, speeding up the $Yb^{3+} \rightarrow Ho^{3+}$ energy-transfer process. As it is affected by the migration of $Yb^{3+}$ ions, the energy-transfer coefficient $C_1$ exhibits a linear dependence on the $Yb^{3+}$ concentration.

As demonstrated by Equation (5), the green emission intensity can be obtained by $I_4 = \gamma_4 n_4 = C_3\gamma_4\tau_4 I_1 I_2$ and, because the cross relaxation of the Ho–Ho interaction is not considered, the lifetime, $\tau_4$, is a constant for fixed $Yb^{3+}$ concentrations. $\tau_4$ is measured to be 54.5 μs (±5%) in $CaSc_2O_4$:0.2%$Ho^{3+}$,10%$Yb^{3+}$. $I_4$ can be calculated according to the infrared emission spectra in Figure 3. The calculated $I_4$ values at various $Ho^{3+}$ concentrations are presented in Figure 9, scaled to the maximum. For comparison, the $I_4$ values obtained directly from the UCL emission spectra are also detailed. The calculated and experimental $I_4$ trends are consistent with each other, demonstrating the validity of both the theoretical analyses and experimental data.

The decay curves of $Yb^{3+}$:$^2F_{5/2} \rightarrow {}^2F_{7/2}$ emission in $CaSc_2O_4$:x$Ho^{3+}$,10%$Yb^{3+}$ ($x = 0$, 0.05, 0.1, 0.2, 0.4, and 0.8%) are shown in Figure 10. The $Yb^{3+}$ singly doped $CaSc_2O_4$ sample exhibits a single exponential decay. When $Ho^{3+}$ is co-doped, the decays rapidly speed-up, reflecting efficient $Yb^{3+} \rightarrow Ho^{3+}$ energy transfer. The energy-transfer efficiency ($\eta_{ET}$) can be calculated by $\eta_{ET} = 1 - \tau_{Yb}/\tau_{Yb0}$, in which $\tau_{Yb0}$ and $\tau_{Yb}$ represent the lifetime of $Yb^{3+}$:$^2F_{5/2}$ in $Yb^{3+}$ singly doped $CaSc_2O_4$ and $Ho^{3+}$/$Yb^{3+}$ in co-doped $CaSc_2O_4$ samples, respectively. The inset shows that $\eta_{ET}$ increases, before finally reaching a saturation state. The $\eta_{ET}$ approaches 50% for the concentration-optimized

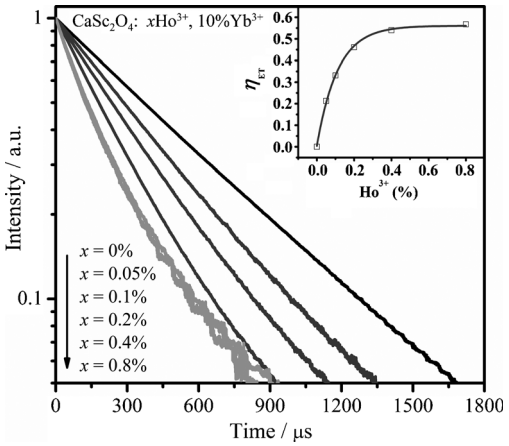


**Figure 10.** Decay curves of $Yb^{3+}$:$^2F_{5/2} \rightarrow {}^2F_{7/2}$ in $CaSc_2O_4$:x$Ho^{3+}$,10%$Yb^{3+}$ ($x = 0.05$, 0.1, 0.2, 0.4, and 0.8%) under pulsed 980 nm excitation. Inset: $Yb^{3+} \rightarrow Ho^{3+}$ energy-transfer efficiency ($\eta_{ET}$) with different $Ho^{3+}$ concentrations.

sample, that is, $CaSc_2O_4$:0.2%$Ho^{3+}$,10%$Yb^{3+}$. Considering the limit of our lifetime-measurement equipment, of which the response is insensitive to NIR emissions, the real $\eta_{ET}$ is larger than the experimental data.

Figure 11 shows the $Ho^{3+}$ concentration dependence of the $^5I_6$-level lifetime under the pulsed 980 nm excitation. The long-lived $^5I_6$ level exhibits a single exponential decay, indicating no back-energy transfer from $Ho^{3+}$ to $Yb^{3+}$. The lifetime decreases from 1049 to 825 μs with increasing $Ho^{3+}$ concentration, suggesting that the multiphonon relaxation rate, $W_{n21}$, rises slightly. According to Equations (2)–(4), the intensity ratio ($I_3/I_4$) of red-to-green emissions can be expressed by Equation (8):

$$\frac{I_3}{I_4} = \frac{\gamma_3 n_3}{\gamma_4 n_4} = \frac{C_2\gamma_3\tau_3 W_{n21}}{C_3\gamma_4\tau_4\tau_1^{-1} + C_3C_2\gamma_4\tau_4 N_1} \quad (8)$$

It shows $I_3/I_4$ is proportional to $W_{n21}$. The enlarged $W_{n21}$ makes the relative intensity of red emission increase slightly as $Ho^{3+}$ concentration increasing in Figure 3b.

© 2013 Wiley-VCH Verlag GmbH & Co. KGaA, Weinheim

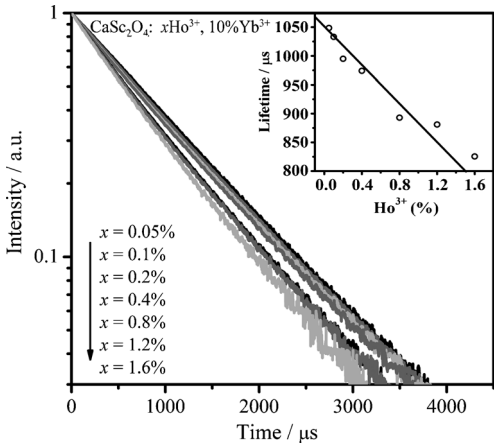


**Figure 11.** Decay curves of $Ho^{3+}$:$^5I_6 \rightarrow {}^5I_8$ in $CaSc_2O_4$:$xHo^{3+}$,10%$Yb^{3+}$ ($x = 0.05$, 0.1, 0.2, 0.4, 0.8, 1.2, and 1.6%) under pulsed 980 nm excitation. Inset: concentration dependence of $^5I_6$ lifetime.

### 2.6 Monochromaticity

The concentration-optimized sample has a strong green emission accompanied with a weak red emission, showing perfect green monochromaticity. Figure 12 shows the normalized UCL

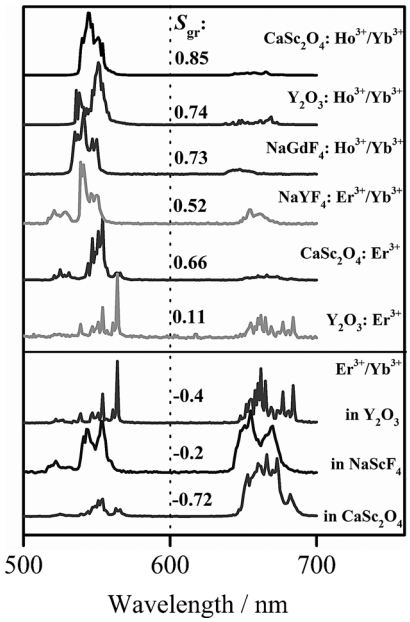


**Figure 12.** Normalized UCL spectra of a number of typical oxide and fluoride materials doped with $Yb^{3+}$, $Ho^{3+}$, or $Er^{3+}$ ions, under 980 nm excitation.

spectra of typical doped oxide and fluoride materials under 980 nm excitation. $CaSc_2O_4$:$Ho^{3+}$/$Yb^{3+}$ exhibited the least-red component in the series of spectra. To compare the spectral purity quantificationally, we introduced a parameter, $S_{gr}$, according to the definition in Ref. [9] [Eq.(9)]:

$$S_{gr} = \frac{A_g - A_r}{A_g + A_r} \quad (9)$$

in which $A_g$ and $A_r$ are the integrated areas of the green emission from 500 to 600 nm and the red emission from 600 to 700 nm, respectively. The pure green emission corresponds to $S_{gr} = 1$. The commercial $NaYF_4$:$Er^{3+}$/$Yb^{3+}$ sample, recognized as one of the most efficient green UCL materials, exhibits weaker green monochromaticity ($S_{gr} = 0.52$), owing to two dominant green and red emission peaks of $Er^{3+}$. The estimated $S_{gr}$ value of $Y_2O_3$:$Ho^{3+}$/$Yb^{3+}$, as good pure green UC emitter, is only about 0.74.[30] The $CaSc_2O_4$:$Ho^{3+}$/$Yb^{3+}$ sample gives rise to the purest green emission, $S_{gr} = 0.85$, which is close to the highest value for $NaYF_4$:$Er^{3+}$/$Pr^{3+}$ ($S_{gr} = 0.88$).[3] The spectrally pure green emission of the $CaSc_2O_4$:$Ho^{3+}$/$Yb^{3+}$ sample suggests that it is a promising candidate for biological imaging and fluorescent labeling with multiple upconverting probes.

## 3. Conclusions

The optical properties of $CaSc_2O_4$:$Ho^{3+}$/$Yb^{3+}$ have been investigated as a function of doping concentration. The $CaSc_2O_4$:0.2%$Ho^{3+}$,10%$Yb^{3+}$ sample was optimized for the strongest green UCL, and it presents perfect green monochromaticity as $S_{gr} = 0.85$, which approaches the highest reported value $S_{gr} = 0.88$ for $NaYF_4$:$Er^{3+}$/$Pr^{3+}$. Efficient $Yb^{3+} \rightarrow Ho^{3+}$ energy transfer was observed, and the $\eta_{ET}$ reached 50% for $CaSc_2O_4$:0.2%$Ho^{3+}$,10%$Yb^{3+}$.

The studies of spectral distribution, power dependence, and lifetime measurements revealed the UCL mechanism involved in $CaSc_2O_4$:$Ho^{3+}$/$Yb^{3+}$. The intensity ratio of green-to-NIR emission did not vary with the excitation wavelengths or doping concentrations. Both emissions exhibited the same time evolutions and pump power dependency under 980 nm excitation. We concluded that the green and NIR emissions came from the same upper levels ($^5F_4 + {}^5S_2$). The evolution of the green intensity by experimental methods was in good agreement with the theoretical calculation based on infrared spectral distributions, illustrating it is populated through the $Yb^{3+}$:$^2F_{5/2} + Ho^{3+}$:$^5I_6 \rightarrow Yb^{3+}$:$^2F_{7/2} + Ho^{3+}$:($^5F_4 + {}^5S_2$) pathway. The red emission occurred from the $Ho^{3+}$:$^5F_5$ level. The $^5F_5$ state was populated through $^5I_6 \rightarrow {}^5I_7$ nonradiative relaxation and subsequent $Yb^{3+}$:$^2F_{5/2} + Ho^{3+}$:$^5I_7 \rightarrow Yb^{3+}$:$^2F_{7/2} + Ho^{3+}$:$^5F_5$ energy transfer. The slope $n$ of the red emission was smaller than that of the green emission with long-lived $^5I_7$ as its intermediate level. The relative intensity of red-to-green emissions was dependent upon the multiphonon relaxation rate, $W_{n21}$, of $^5I_6 \rightarrow {}^5I_7$, which experiences a slight enhancement with increasing $Ho^{3+}$ concentration. The results obtained could be well-understood by theoretical analyses based on steady-state rate equations.

## Experimental Section

### Sample Preparation

The series of samples with the general formula $CaSc_{2-x-y}O_4$:$xHo^{3+}$,$yYb^{3+}$ ($0.05\% \le x \le 1.6\%$, $1\% \le y \le 26\%$) were prepared through a solid-state reaction.[18] The constituent carbonate or oxides $CaCO_3$ (99.9%), $Sc_2O_3$ (99.99%), $Yb_2O_3$ (99.99%), and $Ho_2O_3$ (99.99%) were employed as the raw materials, which were mixed homogeneously

© 2013 Wiley-VCH Verlag GmbH & Co. KGaA, Weinheim

by an agate mortar for 30 min, placed in a crucible with a lid, and then sintered at 1500 °C for 4 h.

### Measurements and Characterization

Powder XRD data was collected by using CuKα radiation ($\lambda =$ 1.54056 Å) on a Bruker D8 Advance diffractometer. The Rietveld refinement of the XRD pattern was implemented by using the Fullprof program.[19] The measurements of UCL and infrared spectra were performed by using a Triax 550 spectrometer (Jobin–Yvon), pumped with a power-controllable 980 nm laser diode. In fluorescence lifetime measurements, an optical parametric oscillator (OPO) was tuned to 980 nm as an excitation source, and the signals were detected by using a Tektronix digital oscilloscope (TDS 3052).

## Acknowledgements

*This work is supported by the National Natural Science Foundation of China (10834006, 51172226, 61275055, 11274007, 11174278) and the Natural Science Foundation of Jilin province (201205024).*

**Keywords:** dynamics · energy transfer · fluorescent probes · luminescence · phosphors

[1] Z. G. Chen, H. L. Chen, H. Hu, M. X. Yu, F. Y. Li, Q. Zhang, Z. G. Zhou, T. Yi, C. H. Huang, *J. Am. Chem. Soc.* **2008**, *130*, 3023 – 3029.
[2] M. Nyk, R. Kumar, T. Y. Ohulchanskyy, E. J. Bergey, P. N. Prasad, *Nano Lett.* **2008**, *8*, 3834 – 3838.
[3] E. M. Chan, G. Han, J. D. Goldberg, D. J. Gargas, A. D. Ostrowski, P. J. Schuck, B. E. Cohen, D. J. Milliron, *Nano Lett.* **2012**, *12*, 3839 – 3845.
[4] G. Y. Chen, Y. G. Zhang, G. Somesfalean, Z. G. Zhang, Q. Sun, F. P. Wang, *Appl. Phys. Lett.* **2006**, *89*, 163105.
[5] J. Ryu, H. Park, K. Kim, H. Kim, J. H. Yoo, M. Kang, K. Im, R. Grailhe, R. Song, *J. Phys. Chem. C* **2010**, *114*, 21077 – 21082.
[6] M. J. Dejneka, A. Streltsov, S. Pal, A. G. Frutos, C. L. Powell, K. Yost, P. K. Yuen, U. Müller, J. Lahiri, *Proc. Natl. Acad. Sci. USA* **2003**, *100*, 389 – 393.
[7] J. A. Capobianco, J. C. Boyer, F. Vetrone, A. Speghini, M. Bettinelli, *Chem. Mater.* **2002**, *14*, 2915 – 2921.
[8] E. D. Rosa, P. Salas, H. Desirena, C. Angeles, R. A. Rodríguez, *Appl. Phys. Lett.* **2005**, *87*, 241912.
[9] F. Lahoz, I. R. Martín, A. Briones, *J. Appl. Phys.* **2004**, *95*, 2957 – 2962.
[10] I. R. Martín, V. D. Rodríguez, V. Lavín, U. R. Rodríguez-Mendoza, *J. Alloys Compd.* **1998**, *275 – 277*, 345 – 348.
[11] E. Osiac, I. Sokólska, S. Kück, *Phys. Rev. B* **2002**, *65*, 235119.
[12] J. Li, Z. D. Hao, X. Zhang, Y. S. Luo, J. H. Zhao, S. Z. Lü, J. Cao, J. H. Zhang, *J. Colloid Interface Sci.* **2013**, *392*, 206 – 212.
[13] B. Dong, B. S. Cao, Y. Y. He, Z. Liu, Z. P. Li, Z. Q. Feng, *Adv. Mater.* **2012**, *24*, 1987 – 1993.
[14] B. P. Singh, A. K. Parchur, R. K. Singh, A. A. Ansari, P. Singh, S. B. Rai, *Phys. Chem. Chem. Phys.* **2013**, *15*, 3480 – 3489.
[15] J. R. Carter, R. S. Feigelson, *J. Am. Ceram. Soc.* **1964**, *47*, 141 – 144.
[16] J. Li, J. H. Zhang, Z. D. Hao, X. Zhang, J. H. Zhao, Y. S. Luo, *Appl. Phys. Lett.* **2012**, *101*, 121905.
[17] J. Li, J. H. Zhang, Z. D. Hao, X. Zhang, J. H. Zhao, Y. S. Luo, *J. Appl. Phys.* **2013**, *113*, 223507.
[18] Z. D. Hao, J. H. Zhang, X. Zhang, X. J. Wang, *Opt. Mater.* **2011**, *33*, 355 – 358.
[19] J. Rodríguez-Carvajal, *Physica B.* **1993**, *192*, 55 – 69.
[20] R. D. Shannon, *Acta Crystallogr.* **1976**, *A32*, 751 – 767.
[21] J. Silver, E. Barrett, P. J. Marsh, R. Withnall, *J. Phys. Chem. B* **2003**, *107*, 9236 – 9242.
[22] S. Guy, *Phys. Rev. B* **2006**, *73*, 144101.
[23] B. Peng, T. Izumitani, *Opt. Mater.* **1995**, *4*, 701 – 711.
[24] N. M. Sangeetha, F. C. Veggel, *J. Phys. Chem. C* **2009**, *113*, 14702 – 14707.
[25] M. Pollnau, D. R. Gamelin, S. R. Lüthi, H. U. Güdel, M. P. Hehlen, *Phys. Rev. B* **2000**, *61*, 3337 – 3346.
[26] S. H. Huang, S. T. Lai, L. R. Lou, W. Y. Jia, W. M. Yen, *Phys. Rev. B* **1981**, *24*, 59 – 63.
[27] G. D. Gilliland, R. C. Powell, *Phys. Rev. B* **1988**, *38*, 9958 – 9973.
[28] Y. Yu, Y. D. Zheng, F. Qin, Z. M. Cheng, C. B. Zheng, Z. G. Zhang, W. W. Cao, *J. Lumin.* **2011**, *131*, 190 – 193.
[29] S. Balaji, A. K. Mandal, K. Annapurna, *Opt. Mater.* **2012**, *34*, 1930 – 1934.
[30] Y. Q. Sheng, L. L. Xu, J. Liu, D. Zhai, Z. G. Zhang, *J. Lumin.* **2010**, *130*, 338 – 341.

Received: September 11, 2013
Published online on November 8, 2013

© 2013 Wiley-VCH Verlag GmbH & Co. KGaA, Weinheim